

Train Like a (Var)Pro: Efficient Training of Neural Networks with Variable Projection*

Elizabeth Newman[†], Lars Ruthotto[‡], Joseph Hart[§], and Bart van Bloemen Waanders[¶]

Abstract. Deep neural networks (DNNs) have achieved state-of-the-art performance across a variety of traditional machine learning tasks, e.g., speech recognition, image classification, and segmentation. The ability of DNNs to efficiently approximate high-dimensional functions has also motivated their use in scientific applications, e.g., to solve partial differential equations (PDE) and to generate surrogate models. In this paper, we consider the supervised training of DNNs, which arises in many of the above applications. We focus on the central problem of optimizing the weights of the given DNN such that it accurately approximates the relation between observed input and target data. Devising effective solvers for this optimization problem is notoriously challenging due to the large number of weights, non-convexity, data-sparsity, and non-trivial choice of hyperparameters. To solve the optimization problem more efficiently, we propose the use of variable projection (VarPro), a method originally designed for separable nonlinear least-squares problems. Our main contribution is the Gauss-Newton VarPro method (GNvpro) that extends the reach of the VarPro idea to non-quadratic objective functions, most notably, cross-entropy loss functions arising in classification. These extensions make GNvpro applicable to all training problems that involve a DNN whose last layer is an affine mapping, which is common in many state-of-the-art architectures. In numerical experiments from classification and surrogate modeling, GNvpro not only solves the optimization problem more efficiently but also yields DNNs that generalize better than commonly-used optimization schemes.

Key words. numerical optimization, deep learning, neural networks, variable projection, hyperspectral segmentation, PDE surrogate modeling

1. Introduction. Deep neural networks (DNNs) have emerged as one of the most promising machine learning methods by achieving state-of-the-art performance in a wide range of tasks such as speech recognition [27], image classification [34], and segmentation [50]; for a general introduction to DNNs, see [21]. In the last few years, these successes have also motivated the use of DNNs in scientific applications, for example, to solve partial differential equations (PDEs) [25, 48, 55, 58] and to generate PDE surrogate models [57].

A key contributor to DNNs' success across these applications is their universal approximation properties [11] as well as recent advances in computational hardware, maturity of machine learning software, and the availability of data. However, in practice, training DNNs remains a challenging art that requires careful hyper-parameter tuning and architecture selection. Mathematical insights are critical to overcome some of these challenges and to create principled learning approaches. In this paper, we leverage methods and algorithms from computational science to design a reliable, practical tool to train DNNs efficiently and effectively.

*Submitted to the editors on December 22, 2024.

Funding: LR's and EN's work was supported by Sandia Contract 2003941 and NSF DMS 1751636.

[†]Department of Mathematics, Emory University, Atlanta, GA, USA (elizabeth.newman@emory.edu, <http://math.emory.edu/~enewma5/>).

[‡]Departments of Mathematics and Computer Science, Emory University, Atlanta, GA, USA, (lruthotto@emory.edu, <http://math.emory.edu/~lruthot/>)

[§]Sandia National Laboratories, Albuquerque, NM, USA

[¶]Sandia National Laboratories, Albuquerque, NM, USA

DNNs are parameterized mappings between input-target pairs, (\mathbf{y}, \mathbf{c}) . Learning means finding the weights of the mapping to achieve accurate approximations of the input-target relationships. In supervised learning, the weights of the mapping are computed by minimizing an expected loss or discrepancy of $G(\mathbf{y}) \approx \mathbf{c}$ approximated using labeled training data. This optimization problem is difficult because the number of weights and examples is typically large, the objective function is non-convex, and the final weights must generalize beyond the final training data. The latter motivates the use of explicit (e.g., weight-decay or Tikhonov) or implicit (e.g., early stopping of iterative methods) regularization.

Devising effective solvers for the optimization problem has received a lot of attention and two predominant iterative approaches have emerged: stochastic approximation schemes [49], such as stochastic gradient descent (SGD) (or variants like ADAM [32]), and stochastic average approximation (SAA) schemes [33]. Each step of SGD approximates the gradient of the expected loss with a small, randomly-chosen batch of examples that are used to update the DNN weights. Under suitable choices of the step size, also called the learning rate, each step reduces the expected loss and the iterations have been shown empirically to often converge to global minimizers that generalize well. In practice, however, it can be difficult to determine the most effective SGD variants and tune hyperparameters such as the learning rate. Furthermore, even if the scheme converges, the rate is often slow and the sequential nature of the method complicates parallel implementation. Finally, it is non-trivial to incorporate curvature information [5, 36, 60]. An alternative to SGD approaches is minimizing a sample average approximation (SAA) of the objective function, which attempts to overcome some of the aforementioned disadvantages. The accuracy of the average approximation improves with larger batch sizes and can be further increased by repeated sampling [40, 33]. While the computational complexity of a step is proportional to the batch size, larger batches provide more potential for data parallelism. The resulting optimization problem can be solved using deterministic methods including inexact Newton schemes [4, 43, 59]. Particularly the examples in [43] show the competitiveness of Newton-Krylov methods to common SGD approaches in terms of computational cost and generalization.

Our goal is to further improve the efficiency of SAA methods by exploiting the structure of the DNN architecture. Many state-of-the-art DNNs [26, 48, 35, 34, 50] can be expressed in a separable form

$$(1.1) \quad G(\mathbf{y}, \mathbf{W}, \boldsymbol{\theta}) = \mathbf{W}F(\mathbf{y}, \boldsymbol{\theta}).$$

Here, \mathbf{W} are the parameters of a linear transformation and $\boldsymbol{\theta}$ parameterize the nonlinear feature extractor F . The key idea in this paper is to exploit the separable structure by eliminating the linear parameters through partial optimization. This reduces G to

$$(1.2) \quad G_{\text{red}}(\mathbf{y}, \boldsymbol{\theta}) = \mathbf{W}(\boldsymbol{\theta})F(\mathbf{y}, \boldsymbol{\theta}),$$

where $\mathbf{W}(\boldsymbol{\theta})$ denotes the optimal linear transformation for the current feature extractor $F(\cdot, \boldsymbol{\theta})$. For example, for least-squares loss functions, $\mathbf{W}(\boldsymbol{\theta})F(\mathbf{y}, \boldsymbol{\theta})$ is the projection of the target feature \mathbf{c} onto the subspace spanned by the nonlinear feature extractor. Hence, the resulting scheme is known as variable projection (VarPro); for the original works, see [19, 29] and for excellent surveys refer to [20, 42].

VarPro has been widely used to solve separable, nonlinear least-squares problems (see [20] and references therein), and its first applications to DNNs, to our best knowledge, can be attributed to [56, 46]. These works train relatively shallow neural networks as function approximators and therefore use a regression loss function. In addition to the obvious advantage of reducing the number of weights, these works also show that VarPro can create more accurate models and can accelerate the training process. The analysis in [56] reveals that the faster rate of convergence can be explained by the improved conditioning of the optimization problem. Another advantage of VarPro is its ability to capture the coupling between the variables \mathbf{W} and $\boldsymbol{\theta}$, which is to be expected in our application. In the presence of tight coupling between these blocks, VarPro can outperform block coordinate descent approaches (see, e.g., [10] for a detailed comparison for an imaging problem). Using block coordinate descent to train neural networks has recently been proposed in [45, 12].

Our main contribution is the development of a Gauss-Newton-Krylov implementation of VarPro (GNvpro) that extends its use beyond least-squares functions, specifically to cross-entropy loss functions arising in classification. For cross-entropy loss functions, there is no closed-form expression for $\mathbf{W}(\boldsymbol{\theta})$, and therefore, to compute (1.2) efficiently and robustly, we develop a tailored trust region Newton scheme. Due to our efficient implementation of this scheme the overhead of computing $\mathbf{W}(\boldsymbol{\theta})$ is negligible in practice and the computational cost of DNN training is dominated by forward and backward passes through the feature extractor. We compute the Jacobian of $\mathbf{W}(\boldsymbol{\theta})$, which is required in GNvpro, using implicit differentiation and accelerate the computation by re-using (low-rank) factorizations. As these two steps are independent of the choice of F , GNvpro is applicable to a general class of DNN architecture. To demonstrate its versatility, we experiment with the network architecture and as learning tasks consider classification, segmentation, and PDE surrogate modeling. Across those examples and as expected, GNvpro accelerates the convergence of the optimization problem compared to Gauss-Newton-Krylov schemes that train (1.1) and SGD variants. Equally important, DNNs are trained that generalize well. GNvpro's ability to train a relatively small DNN to high accuracy is particularly attractive for surrogate modeling as the goal here is to reduce the computational cost of expensive PDE solves.

Before deriving our algorithm, we establish a geometric intuition of VarPro and highlight the effectiveness of GNvpro through a simple binary classification example in Figure 1. Our data consists of input-target pairs (\mathbf{y}, c) where $\mathbf{y} \in \mathbb{R}^2$ are points lying in the Cartesian plane belonging to one of two classes: contained in an ellipse ($c = 0$) or outside the ellipse ($c = 1$). We train a network with a three-layer feature extractor, written as the composition

$$F(\mathbf{y}, \boldsymbol{\theta}) = \sigma(\mathbf{K}_2 \sigma(\mathbf{K}_1 \sigma(\mathbf{K}_0 \mathbf{y} + \mathbf{b}_0) + \mathbf{b}_1) + \mathbf{b}_2),$$

where the matrices are of size $\mathbf{K}_0 \in \mathbb{R}^{4 \times 2}$, $\mathbf{K}_1 \in \mathbb{R}^{4 \times 4}$, and $\mathbf{K}_2 \in \mathbb{R}^{2 \times 4}$, the vectors are of size $\mathbf{b}_0 \in \mathbb{R}^4$, $\mathbf{b}_1 \in \mathbb{R}^4$, and $\mathbf{b}_2 \in \mathbb{R}^2$, and the activation function $\sigma(x) = \tanh(x)$ acts entry-wise. For notational convenience, we let $\boldsymbol{\theta} = (\mathbf{K}_0, \mathbf{b}_0, \mathbf{K}_1, \mathbf{b}_1, \mathbf{K}_2, \mathbf{b}_2)$ be a vector containing all of the trainable weights. We use our trust region Gauss-Newton-Krylov and Tikhonov regularization with and without VarPro to compare optimization strategies. As illustrated in Figure 1, GNvpro improves the accuracy and efficiency and illustrates a near-optimal geometric evolution throughout the iteration history.

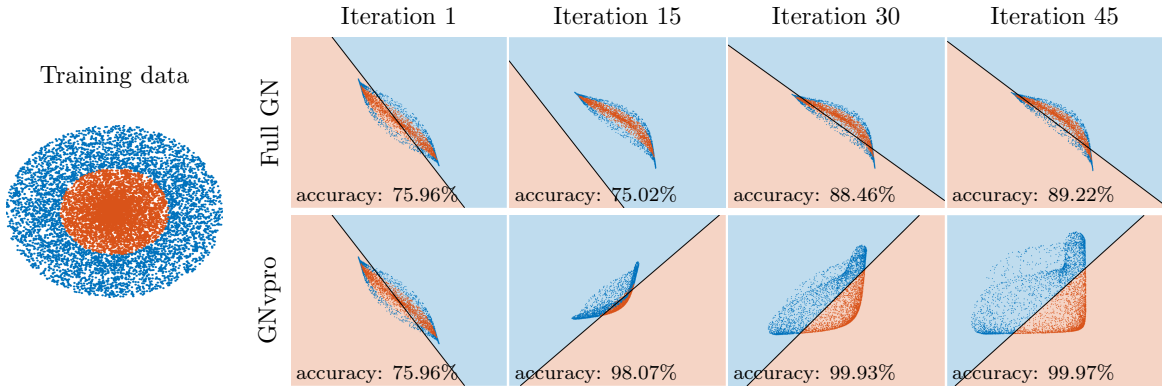


Figure 1. We compare the training performance of the full model (top row) and the VarPro-reduced model (bottom) given by (1.1) and (1.2), respectively, for a two-dimensional binary classification problem. The training data consists of inputs $\mathbf{y} \in \mathbb{R}^2$ and are visualized in the left figure using red and blue dots based on their label $c \in \{0, 1\}$. In the other panels, we display the transformed training data $F(\mathbf{y}, \boldsymbol{\theta})$ at intermediate optimization iterations, the linear classifier \mathbf{W} via a black line, and the resulting classification via the background shading. By design, each iteration of VarPro uses the optimal linear classifier for the transformed data and thus converges quicker and to a more accurate solution.

The paper is organized as follows. In Section 2, we derive GNvpro and its components by generalizing the VarPro idea to cross-entropy loss functions and in particular discuss the effective solution of the partial minimization problem arising in classification problems. In Section 3, we provide three numerical examples consisting of two least-squares regression problems and one image segmentation problem. The regression problems seek to train a DNN surrogate models of the parameter-to-observable map for two PDEs, Convection Diffusion Reaction and Direct Current Resistivity. The segmentation problem seeks to train a DNN to classify pixels that correspond to different materials or crops in a hyperspectral image. In Section 4, we summarize our findings and discuss future directions.

2. Train like a (Var)Pro. In this section, we present GNvpro, our Gauss-Newton-Krylov implementation of variable projection (VarPro) that enables training separable DNN architectures (1.1) to solve regression and classification problems. Our algorithmic process is predicated on formulating the stochastic optimization problem as a sample average approximation. To implement VarPro, we separate the nonlinear and linear DNN components into outer and inner problems, respectively. At each training iteration, we solve the inner problem to eliminate \mathbf{W} as in (1.2). The type of loss function dictates the choice of the solver for the inner problem: in the case of a least-squares function, an SVD solves the inner problem and in the case for the cross-entropy function, we employ a trust region approach. To efficiently solve the outer problem, we carefully linearize the reduced forward model (1.2) and derive GNvpro as a generalization of Gauss-Newton to non-quadratic loss functions.

2.1. VarPro for DNN Training. Let (\mathbf{y}, \mathbf{c}) be an input-target pair where \mathbf{y} belongs to the feature space $\mathcal{Y} \subset \mathbb{R}^{N_{\text{in}}}$ and \mathbf{c} belongs to the target space $\mathcal{C} \subset \mathbb{R}^{N_{\text{out}}}$. We denote the data set, the set of all input-target pairs, as $\mathcal{D} \subset \mathcal{Y} \times \mathcal{C}$, and assume that it is large or even infinite. In this work, we consider DNN models of the form (1.1), which consist of two

Table 1

Loss functions supported in our framework for training DNNs to solve function approximation (least-squares) and classification tasks (logistic, multinomial). The first argument of the loss functions is the output of the network, i.e., $\mathbf{x} = \mathbf{W}F(\mathbf{y}, \boldsymbol{\theta})$. The softmax function $h(\mathbf{x}) = \exp(\mathbf{x})/(1 + \mathbf{e}^\top \mathbf{x})$ transforms the output into a vector of probabilities where the i^{th} value is the probability of belonging to class i . In the one-dimensional case, the softmax function is equivalent to the sigmoid function. The unit simplex $\Delta^{N_{\text{target}}}$ contains vectors with non-negative entries that sum to 1 (i.e., vectors of probabilities).

Least Squares $L_{\text{ls}} : \mathbb{R}^{N_{\text{target}}} \times \mathbb{R}^{N_{\text{target}}} \rightarrow \mathbb{R}$	$L_{\text{ls}}(\mathbf{x}, \mathbf{c}) = \ \mathbf{x} - \mathbf{c}\ _2^2$
Logistic Regression $L_{\text{log}} : \mathbb{R} \times \{0, 1\} \rightarrow \mathbb{R}$	$L_{\text{log}}(x, c) = -c \log h(x) - (1 - c)^\top \log(1 - h(x))$
Multinomial Regression $L_{\text{mul}} : \mathbb{R}^{N_{\text{target}}} \times \Delta^{N_{\text{target}}} \rightarrow \mathbb{R}$	$L_{\text{mul}}(\mathbf{x}, \mathbf{c}) = -\mathbf{c}^\top \log h(\mathbf{x}) - (\mathbf{e} - \mathbf{c})^\top \log(\mathbf{e} - h(\mathbf{x}))$

components: a nonlinear, parametrized feature extractor $F : \mathcal{Y} \times \mathbb{R}^{N_\theta} \rightarrow \mathbb{R}^{N_{\text{out}}}$ and a final linear transformation $\mathbf{W} \in \mathbb{R}^{N_{\text{target}} \times N_{\text{out}}}$. We denote the weights of the feature extraction F by $\boldsymbol{\theta} \in \mathbb{R}^{N_\theta}$.

In a supervised setting, we use the labeled data in \mathcal{D} to train the weights of the model. We pose this as the stochastic optimization problem

$$(2.1) \quad \min_{\mathbf{W}, \boldsymbol{\theta}} \mathbb{E}[L(\mathbf{W}F(\mathbf{y}, \boldsymbol{\theta}), \mathbf{c})] + R(\boldsymbol{\theta}) + S(\mathbf{W}),$$

where the loss function $L : \mathbb{R}^{N_{\text{target}}} \times \mathcal{C} \rightarrow \mathbb{R}$ is convex in its first argument, and $R : \mathbb{R}^{N_\theta} \rightarrow \mathbb{R}$ and $S : \mathbb{R}^{N_{\text{target}} \times N_{\text{out}}} \rightarrow \mathbb{R}$ are convex regularizers. In this work, we choose the Tikhonov regularizers $R(\boldsymbol{\theta}) = \frac{\alpha_1}{2} \|\mathbf{B}\boldsymbol{\theta}\|^2$ (where \mathbf{B} is a user-defined regularization operator) and $S(\mathbf{W}) = \frac{\alpha_2}{2} \|\mathbf{W}\|_F^2$ (where $\|\cdot\|_F$ is the Frobenius norm) with fixed parameters $\alpha_1, \alpha_2 > 0$, which are called weight-decay in the machine learning community. The expectation is over the uniform distribution defined by the input-output pairs in \mathcal{D} . We list some loss functions that are commonly-used in DNN training and supported by our framework in [Table 1](#).

We turn (2.1) into a deterministic problem by replacing the expected loss with its sample average approximation (SAA) (see also [33, 40, 31])

$$(2.2) \quad \min_{\mathbf{W}, \boldsymbol{\theta}} \Phi(\mathbf{W}, \boldsymbol{\theta}) \equiv \frac{1}{|\mathcal{T}|} \sum_{(\mathbf{y}, \mathbf{c}) \in \mathcal{T}} L(\mathbf{W}F(\mathbf{y}, \boldsymbol{\theta}), \mathbf{c}) + R(\boldsymbol{\theta}) + S(\mathbf{W}).$$

Here, we partition the labeled data into a training set $\mathcal{D}_{\text{train}}$, a validation set \mathcal{D}_{val} , and a test set $\mathcal{D}_{\text{test}}$, and choose the batch \mathcal{T} from the training set, i.e., $\mathcal{T} \subset \mathcal{D}_{\text{train}} \subset \mathcal{D}$. The validation dataset is used to inform the network design and calibrate the regularization parameters and the test dataset is used to gauge how well the final model generalizes. In SAA methods, generalization can be achieved by choosing a sufficiently large batch size $|\mathcal{T}|$, as this closes the match between (2.1) and (2.2), and by solving a sequence of instances of the deterministic problem with different batches [33].

Although the optimization problem (2.2) can be solved using a variety of deterministic numerical optimization methods, their effectiveness in practice can be disappointing (see top row of Figure 1 as an example). Challenges include the non-convexity of the objective function in θ , immense computational costs in the large-scale setting (i.e., when the number of examples and the number of weights are large), and the coupling between the linear variable \mathbf{W} and the DNN weights θ in (1.1). To derive a more effective approach, we exploit the separability of the DNN model and the convexification of the loss function by eliminating the variables of the linear part of the model to obtain the reduced optimization problem

$$(2.3) \quad \min_{\theta} \Phi_{\text{red}}(\theta) \equiv \Phi(\mathbf{W}(\theta), \theta)$$

$$(2.4) \quad \text{where } \mathbf{W}(\theta) = \arg \min_{\mathbf{W}} \Phi(\mathbf{W}, \theta).$$

Since we eliminated the weights associated with the linear part of the model, we call $\Phi_{\text{red}} : \mathbb{R}^{N_\theta} \rightarrow \mathbb{R}$ the reduced objective function. For the least-squares loss function, this approach is known as variable projection (VarPro) (see [19, 29, 20, 42] and also our discussion in Subsection 2.2), but as we show below the approach extends to other convex loss functions. One of the key practical benefits of VarPro is that the minimization of (2.3) with respect to θ implicitly accounts for the coupling with the eliminated variable \mathbf{W} , which can dramatically accelerate the convergence (see also the discussion and experiments in [10]).

The reduced objective function (2.3) can be minimized using gradient-based optimization, without differentiating the inner problem (2.4). In other words, the gradients of (2.3) and (2.2) with respect to θ are equal, as can be verified via

$$(2.5) \quad \nabla_{\theta} \Phi_{\text{red}}(\theta) \nabla_{\theta} \mathbf{w}(\theta) \nabla_{\mathbf{w}} \Phi(\mathbf{W}(\theta), \theta) \nabla_{\theta} \Phi(\mathbf{W}(\theta), \theta) = \nabla_{\theta} \Phi(\mathbf{W}(\theta), \theta),$$

This observation also implies that gradients can become inaccurate when the inner problem is not solved to sufficient accuracy.

For the loss functions considered in this paper, the inner problem (2.4) is smooth, strictly convex, and of moderate size. Thus, it can be solved efficiently using convex optimization schemes. The method by which we solve the inner optimization problem varies based on the loss function. For regression tasks, we solve the resulting least-squares problem directly using the singular value decomposition (see details in Subsection 2.2) and for the cross-entropy loss functions we solve the convex program iteratively using a Newton-Krylov trust region scheme (see details in Subsection 2.3).

The computational cost of solving (2.4) depends on the number of examples $|\mathcal{T}|$, the width of the network N_{out} , and the number of output features N_{target} . As N_{out} and N_{target} are typically on the order of tens or hundreds, even for large-scale learning tasks and due to our efficient implementations described in the following sections, the cost of solving the convex inner problems (2.4) is minimal in practice. Importantly, these costs grow independent of the depth of the DNN used as a nonlinear feature extractor F . Hence, the cost of evaluating the reduced objective function in (2.3) and its gradient (2.5) depends on the complexity of F . As the depth of F grows, the forward and backward passes through the network dominate the training costs and the overhead of solving (2.3) becomes negligible.

We provide a side-by-side comparison of evaluating the full and reduced objective functions in Algorithm 2.1. The substantial difference is Line 4 in which we solve for the optimal $\mathbf{W}(\theta)$

Algorithm 2.1 Evaluating objective functions

Inputs: Batch $\mathcal{T} = \{(\mathbf{y}_i, \mathbf{c}_i) : i = 1, 2, \dots, |\mathcal{T}|\}$, feature extractor F , weights $\boldsymbol{\theta}$, and, \mathbf{W} (only needed when not using VarPro)

Forward propagate

1: **for** $i = 1, \dots, |\mathcal{T}|$ **do**
2: $\mathbf{z}_i(\boldsymbol{\theta}) = F(\mathbf{y}_i, \boldsymbol{\theta})$
3: **end for**

Evaluate Φ (no VarPro)

4: _____
5: $\Phi_c = \Phi(\mathbf{W}, \boldsymbol{\theta})$
6: $\nabla \Phi_c = \nabla_{(\mathbf{W}, \boldsymbol{\theta})} \Phi(\mathbf{W}, \boldsymbol{\theta})$
7: $J_c = J_{(\mathbf{W}, \boldsymbol{\theta})} \left(\frac{1}{|\mathcal{T}|} \sum_{i=1}^{|\mathcal{T}|} \mathbf{W} \mathbf{z}_i(\boldsymbol{\theta}) \right)$
8: return Φ_c , $\nabla \Phi_c$, and, for GNvpro, J_c

Evaluate Φ_{red} (VarPro)

4: $\mathbf{W}(\boldsymbol{\theta}) = \arg \min_{\mathbf{W}} \Phi(\mathbf{W}, \boldsymbol{\theta})$
5: $\Phi_c = \Phi_{\text{red}}(\boldsymbol{\theta}) \equiv \Phi(\mathbf{W}(\boldsymbol{\theta}), \boldsymbol{\theta})$
6: $\nabla \Phi_c = \nabla_{\boldsymbol{\theta}} \Phi_{\text{red}}(\boldsymbol{\theta})$
7: $J_c = J_{\boldsymbol{\theta}} \left(\frac{1}{|\mathcal{T}|} \sum_{i=1}^{|\mathcal{T}|} \mathbf{W}(\boldsymbol{\theta}) \mathbf{z}_i(\boldsymbol{\theta}) \right)$

based on the current weights to evaluate the reduced objective. Observe that the architecture of the feature extractor is arbitrary, which allows us to experiment with a wide range of architectures, particularly deep networks (see [56] for experiments with single-layer neural networks).

2.2. Efficient Implementation for the Least-Squares Loss. For the least-squares loss function, the inner problem (2.4) is a linear regression problem that we solve directly using the singular value decomposition (SVD). For concreteness, we now outline our implementation for this important special case. Our final scheme is equivalent to the ones derived in [42, 20]. For ease of notation, we arrange the input and target vectors of the current batch $\mathcal{T} \subset \mathcal{D}_{\text{train}}$ column-wise in the matrices $\mathbf{Y} \in \mathbb{R}^{N_{\text{in}} \times |\mathcal{T}|}$ and $\mathbf{C} \in \mathbb{R}^{N_{\text{target}} \times |\mathcal{T}|}$, respectively. Similarly, let the i -th column of $\mathbf{Z}(\boldsymbol{\theta}) = F(\mathbf{Y}, \boldsymbol{\theta}) \in \mathbb{R}^{N_{\text{out}} \times |\mathcal{T}|}$ correspond to output feature $F(\mathbf{y}_i, \boldsymbol{\theta})$, where \mathbf{y}_i is the i -th column of \mathbf{Y} . Using this notation and assuming weight decay regularization, we can write the reduced regression problem compactly as

$$(2.6) \quad \min_{\boldsymbol{\theta}} \Phi_{\text{ls}}(\boldsymbol{\theta}) \equiv \frac{1}{2|\mathcal{T}|} \|\mathbf{W}(\boldsymbol{\theta}) \mathbf{Z}(\boldsymbol{\theta}) - \mathbf{C}\|_F^2 + \frac{\alpha_1}{2} \|\boldsymbol{\theta}\|_2^2 + \frac{\alpha_2}{2} \|\mathbf{W}(\boldsymbol{\theta})\|_F^2$$

$$(2.7) \quad \text{s.t. } \mathbf{W}(\boldsymbol{\theta}) = \arg \min_{\mathbf{W}} \frac{1}{2|\mathcal{T}|} \|\mathbf{W} \mathbf{Z}(\boldsymbol{\theta}) - \mathbf{C}\|_F^2 + \frac{\alpha_2}{2} \|\mathbf{W}\|_F^2.$$

We note that the inner problem is separable by rows and hence the N_{target} rows of $\mathbf{W}(\boldsymbol{\theta})$ can be computed independently and in parallel. We solve the inner optimization problem efficiently and stably using the (reduced) SVD [42, 29] of the network outputs

$$(2.8) \quad \frac{1}{\sqrt{|\mathcal{T}|}} \mathbf{Z}(\boldsymbol{\theta}) = \mathbf{U} \boldsymbol{\Sigma} \mathbf{V}^T,$$

where the columns of $\mathbf{U} \in \mathbb{R}^{N_{\text{out}} \times N_{\text{out}}}$ and $\mathbf{V} \in \mathbb{R}^{|\mathcal{T}| \times N_{\text{out}}}$ are orthonormal and $\boldsymbol{\Sigma} \in \mathbb{R}^{N_{\text{out}} \times N_{\text{out}}}$ is diagonal. Here, we assume the number of samples is greater than the number of output features which is a reasonable assumption when optimizing with SAA methods.

2.3. Efficient Implementation for Cross-Entropy Loss Functions. For the cross-entropy loss functions used in logistic and multinomial regression tasks, the inner problem (2.4) generally does not admit a closed-form solution. For our choice of the regularizer S , the elimination requires solving a smooth and strictly convex problem. Typically, this problem has no more than a few thousand variables. To efficiently solve this problem to high accuracy, we use the Newton-Krylov trust region method described below. We recall that due to (2.5), the convergence of the outer optimization scheme crucially depends on the accuracy of the Newton scheme.

To iteratively solve (2.5), we initialize the weights with $\mathbf{W}^{(0)} \equiv \mathbf{0}$ and a user-specified trust region radius $\Delta^{(0)}$. In the j -th iteration, we compute the update to the weight by approximately solving the quadratic program

$$(2.9) \quad \min_{\delta\mathbf{w}} \nabla_{\mathbf{w}}\Phi(\mathbf{W}^{(j)}, \boldsymbol{\theta})^\top \delta\mathbf{w} + \frac{1}{2} \delta\mathbf{w}^\top \nabla_{\mathbf{w}}^2\Phi(\mathbf{W}^{(j)}, \boldsymbol{\theta}) \delta\mathbf{w} \text{ subject to } \|\delta\mathbf{w}\| \leq \Delta^{(j)}.$$

Although the number of variables, $n_{\mathbf{w}} = N_{\text{target}}N_{\text{out}}$, is modest in most DNN training problems, we improve the efficiency of the overall scheme by projecting this subproblem onto the r -dimensional Krylov subspace $\mathcal{K}_r(\nabla_{\mathbf{w}}^2\Phi(\mathbf{W}^{(j)}, \boldsymbol{\theta}), \nabla_{\mathbf{w}}\Phi(\mathbf{W}^{(j)}, \boldsymbol{\theta}))$. Using the Arnoldi method, this gives a low-rank factorization such that

$$(2.10) \quad \mathbf{Q}_{r+1}\mathbf{H}_r = \nabla_{\mathbf{w}}^2\Phi(\mathbf{W}^{(j)}, \boldsymbol{\theta})\mathbf{Q}_r,$$

where the columns of $\mathbf{Q}_{r+1} \in \mathbb{R}^{n_{\mathbf{w}} \times (r+1)}$ are orthonormal, $\mathbf{Q}_r \in \mathbb{R}^{n_{\mathbf{w}} \times r}$ contains the first r columns of \mathbf{Q}_{r+1} , and $\mathbf{H}_r \in \mathbb{R}^{(r+1) \times r}$ is an upper Hessenberg matrix. As the Hessian is symmetric, \mathbf{H}_r should be tridiagonal; however, this may not be the case in practice due to roundoff errors arising in the computation of matrix-vector products with the Hessian. The rank r is chosen adaptively by stopping the Arnoldi scheme when the estimate of

$$\min_{\mathbf{z} \in \mathbb{R}^r} \frac{\|\mathbf{H}_r \mathbf{z} - \beta \mathbf{e}_1\|}{\beta}, \quad \text{where } \beta = \|\nabla_{\mathbf{w}}\Phi(\mathbf{W}^{(j)}, \boldsymbol{\theta})\|, \quad \mathbf{e}_1 = (1, 0, 0, \dots)^\top \in \mathbb{R}^{r+1}$$

falls below a user-defined tolerance or a user-specified maximum rank, r_{\max} , is reached. We note that, in exact arithmetic, this stopping criteria renders our scheme equivalent to GMRES [53, Sec. 6.5] without restarting when the trust region constraint is inactive.

Using the low-rank factorization (2.10) and replacing the inequality constraints with a quadratic penalty, we obtain the approximate step approximate step $\delta\mathbf{w} = \mathbf{Q}_r \mathbf{z}^*(\lambda)$, where for $\lambda \geq 0$, $\mathbf{z}^*(\lambda) \in \mathbb{R}^r$ is given by

$$\mathbf{z}^*(\lambda) = \arg \min_{\mathbf{z} \in \mathbb{R}^r} \frac{1}{2} \|\mathbf{H}_r \mathbf{z} - \beta \mathbf{e}_1\|^2 + \frac{\lambda}{2} \|\mathbf{z}\|^2.$$

If $\|\mathbf{z}^*(0)\| > \Delta^{(j)}$ (i.e., the trust region constraint is violated), we use MATLAB's `fminsearch` with initial bracket $\left[0, \frac{\beta}{\Delta^{(j)}}\right]$ to find the smallest value of λ such that the trust region constraint holds. Finally, we obtain the trial step $\mathbf{W}_{\text{trial}} = \mathbf{W}^{(j)} + \delta\mathbf{w}$.

To accept or reject the trial step and update the trust region radius, we compare the predicted and actual reduction achieved by $\mathbf{W}_{\text{trial}}$ and follow the guidelines in [30, Sec. 3.3].

We note that the low-rank factorization is only updated when $\mathbf{W}_{\text{trial}}$ is accepted. The Newton scheme is stopped when a maximum number of iteration is reached or when the scheme has converged, defined as

$$\frac{\|\nabla_{\mathbf{w}}\Phi(\mathbf{W}^{(j+1)}, \boldsymbol{\theta})\|}{\|\nabla_{\mathbf{w}}\Phi(\mathbf{W}^{(0)}, \boldsymbol{\theta})\|} \leq \epsilon_{\text{rel}}, \quad \text{or} \quad \|\nabla_{\mathbf{w}}\Phi(\mathbf{W}^{(j+1)}, \boldsymbol{\theta})\| \leq \epsilon_{\text{abs}},$$

where we set the relative and absolute tolerances to $\epsilon_{\text{rel}} = 10^{-10}$ and $\epsilon_{\text{abs}} = 10^{-10}$, respectively.

2.4. GNvpro. To solve the reduced optimization problem (2.3) accurately and efficiently we now present our proposed Gauss-Newton-Krylov implementation of VarPro, GNvpro. We use the trust region scheme described in the previous section to iteratively update the weights $\boldsymbol{\theta}$. Recall that the outer problem generally is not convex.

In the k -th iteration of GNvpro, we build the trust region subproblem using the following approximation of the loss

$$(2.11) \quad \begin{aligned} L(G_{\text{red}}(\mathbf{y}, \boldsymbol{\theta}^{(k)}) + J_{\boldsymbol{\theta}}G_{\text{red}}\delta\boldsymbol{\theta}, \mathbf{c}) \approx \\ L(G_{\text{red}}(\mathbf{y}, \boldsymbol{\theta}^{(k)}), \mathbf{c}) + \nabla L^{\top} J_{\boldsymbol{\theta}}G_{\text{red}}\delta\boldsymbol{\theta} + \frac{1}{2}\delta\boldsymbol{\theta}^{\top} J_{\boldsymbol{\theta}}G_{\text{red}}^{\top} \nabla^2 L J_{\boldsymbol{\theta}}G_{\text{red}}\delta\boldsymbol{\theta}, \end{aligned}$$

where ∇L and $\nabla^2 L$ are, respectively, the gradient and the Hessian of $L(G_{\text{red}}(\mathbf{y}, \boldsymbol{\theta}^{(k)}), \mathbf{c})$ with respect to the first argument, and $J_{\boldsymbol{\theta}}G_{\text{red}} \in \mathbb{R}^{N_{\text{target}} \times N_{\boldsymbol{\theta}}}$ is the Jacobian of the reduced model with respect to $\boldsymbol{\theta}$

$$(2.12) \quad G_{\text{red}}(\mathbf{y}, \boldsymbol{\theta}^{(k)} + \delta\boldsymbol{\theta}) \approx G_{\text{red}}(\mathbf{y}, \boldsymbol{\theta}^{(k)}) + J_{\boldsymbol{\theta}}G_{\text{red}}\delta\boldsymbol{\theta}.$$

We note that our approach is equivalent to the classical Gauss-Newton method for nonlinear least-squares loss when we consider the regression loss. GNvpro uses this approximation of the loss to formulate the trust region subproblem (compare to (2.9)) and uses the same subspace projection, and trust region strategy as above albeit with larger tolerances.

We now derive the Jacobian of the VarPro reduced model, $J_{\boldsymbol{\theta}}G_{\text{red}}$, that appears in (2.12). Applying the product rule to (1.2), the Jacobian of the reduced DNN model reads

$$(2.13) \quad J_{\boldsymbol{\theta}}G_{\text{red}}(\mathbf{y}, \boldsymbol{\theta}) = J_{\boldsymbol{\theta}}(\mathbf{W}(\boldsymbol{\theta})F(\mathbf{y}, \boldsymbol{\theta})) = \mathbf{W}(\boldsymbol{\theta})J_{\boldsymbol{\theta}}F(\mathbf{y}, \boldsymbol{\theta}) + (F(\mathbf{y}, \boldsymbol{\theta})^{\top} \otimes \mathbf{I}_{N_{\text{target}}})J_{\boldsymbol{\theta}}\mathbf{w}(\boldsymbol{\theta})$$

where \otimes is the Kronecker product and $\mathbf{I}_{N_{\text{target}}}$ is the $N_{\text{target}} \times N_{\text{target}}$ identity matrix [47]. While the Jacobian of the network in the first term can be computed easily using automatic differentiation or using the chain rule, the second term is less trivial as it requires the Jacobian of the (vectorized) solution of the convex problem (2.4). We compute this term by implicitly differentiating the first order necessary condition $\nabla_{\mathbf{w}}\Phi(\mathbf{W}(\boldsymbol{\theta}), \boldsymbol{\theta}) = \mathbf{0}$, which yields

$$(2.14) \quad \mathbf{0} = \nabla_{\mathbf{w}}^2\Phi(\mathbf{W}(\boldsymbol{\theta}), \boldsymbol{\theta})J_{\boldsymbol{\theta}}\mathbf{w}(\boldsymbol{\theta}) + J_{\boldsymbol{\theta}}\nabla_{\mathbf{w}}\Phi(\mathbf{W}(\boldsymbol{\theta}), \boldsymbol{\theta})$$

$$(2.15) \quad \Leftrightarrow J_{\boldsymbol{\theta}}\mathbf{w}(\boldsymbol{\theta}) = -\nabla_{\mathbf{w}}^2\Phi(\mathbf{W}(\boldsymbol{\theta}), \boldsymbol{\theta})^{-1}J_{\boldsymbol{\theta}}\nabla_{\mathbf{w}}\Phi(\mathbf{W}(\boldsymbol{\theta}), \boldsymbol{\theta}).$$

Here, we note that the Hessian $\nabla_{\mathbf{w}}^2\Phi(\mathbf{W}(\boldsymbol{\theta}), \boldsymbol{\theta})$ is positive definite due to the strict convexity of the objective function in \mathbf{W} .

Finally, we note that matrix-vector products with $J_{\theta}G_{\text{red}}(\mathbf{y}, \theta)$ and its transpose can be performed without the (costly) Kronecker product, that is, for vectors $\delta\theta \in \mathbb{R}^{N_{\theta}}$ and $\delta s \in \mathbb{R}^{N_{\text{out}}}$ we have

$$(2.16) \quad J_{\theta}G_{\text{red}}\delta\theta = \mathbf{W}(\theta)(J_{\theta}F(\mathbf{y}, \theta)\delta\theta) + (J_{\theta}\mathbf{w}(\theta)\delta\theta)F(\mathbf{y}, \theta)$$

$$(2.17) \quad J_{\theta}G_{\text{red}}^{\top}\delta s = J_{\theta}F(\mathbf{y}, \theta)^{\top}(\mathbf{W}(\theta)^{\top}\delta s) + J_{\theta}\mathbf{w}(\theta)^{\top}(\text{vec}(\delta s F(\mathbf{y}, \theta)^{\top})).$$

When (2.15) is solved efficiently, the cost of the matrix-vector products is dominated by the linearized forward or backward propagations through the feature extractor F . We now provide efficient implementations of the Jacobian matrix-vector product for the least-squares and the cross-entropy loss, respectively.

Jacobian for Least-Squares Loss. We can simplify the Jacobian $J_{\theta}\mathbf{W}(\theta)$ in (2.15) using the SVD of $\mathbf{Z}(\theta)$ computed in (2.8). Denoting the residual by $\mathbf{R}(\theta) = \mathbf{W}(\theta)\mathbf{Z}(\theta) - \mathbf{C}$, we note that

$$(2.18) \quad \nabla_{\mathbf{W}}^2\Phi_{\text{ls}}(\mathbf{W}(\theta), \theta) = \mathbf{U}(\Sigma^2 + \alpha_2\mathbf{I}_{N_{\text{out}}})^{-1}\mathbf{U}^{\top}$$

$$(2.19) \quad J_{\theta}\nabla_{\mathbf{W}}\Phi_{\text{ls}}(\mathbf{W}(\theta), \theta) = \frac{1}{\sqrt{|\mathcal{T}|}}\mathbf{W}(\theta)J_{\theta}\mathbf{Z}(\theta)\mathbf{V}\Sigma\mathbf{U}^{\top} + \frac{1}{|\mathcal{T}|}\mathbf{R}(\theta)J_{\theta}\mathbf{Z}(\theta)^{\top}$$

With these ingredients, the multiplication of a given vector $\delta\theta \in \mathbb{R}^{N_{\theta}}$ with the Jacobian, for example, simplifies to

$$(2.20) \quad J_{\theta}\mathbf{W}(\theta)\delta\theta = -\left(\frac{1}{\sqrt{|\mathcal{T}|}}\mathbf{W}(\theta)\delta\mathbf{Z}\mathbf{V}\Sigma + \frac{1}{|\mathcal{T}|}\mathbf{R}(\theta)\delta\mathbf{Z}^{\top}\mathbf{U}\right)(\Sigma^2 + \alpha_2\mathbf{I}_{N_{\text{out}}})^{-1}\mathbf{U}^{\top},$$

where we abbreviate the directional derivative of the feature extractor by $\delta\mathbf{Z} = J_{\theta}\mathbf{Z}(\theta)\delta\theta$ and cancel redundant terms. Note that multiplying the inverse Hessian from the right avoids forming the Kronecker product and enables parallel computation of all the rows. The computation of matrix vector products with the transpose of the Jacobian is along the same lines. Efficient implementations of (2.20) re-use the previously-computed SVD from (2.8) to compute $J_{\theta}\mathbf{W}(\theta)$ and also evaluate the Jacobian of the feature extractor $J_{\theta}\mathbf{Z}(\theta)$ only once.

Jacobian for Cross-Entropy Loss. Our implementation of GNvpro re-uses the low-rank decomposition of $\nabla_{\mathbf{W}}^2\Phi(\mathbf{W}(\theta), \theta)$ computed in the last iteration of the inner trust region solve to accelerate matrix-vector products with the Jacobian. That is, we replace (2.15) by $-(\mathbf{Q}_r\mathbf{H}_r^{\dagger}\mathbf{Q}_{r+1}^{\top})J_{\theta}\nabla_{\mathbf{W}}\Phi(\mathbf{W}(\theta), \theta)$, where \mathbf{H}_r^{\dagger} is the Moore-Penrose inverse. To increase the efficiency of computing matrix-vector products our implementation is based on performing a SVD of \mathbf{H}_r and to derive a low-rank factorization of $\mathbf{Q}_r\mathbf{H}_r^{\dagger}\mathbf{Q}_{r+1}^{\top}$ and its transpose. While it can be more accurate to use an iterative method in this step, we did not observe any negative effects on accuracy in our experiments. Moreover, by this choice we ensure that $J_{\theta}G_{\text{red}}$ and $J_{\theta}G_{\text{red}}^{\top}$ given by (2.16) and (2.17), respectively, are transposes of one another for any choice of r .

3. Numerical Experiments. We provide numerical experiments that demonstrate the efficacy of training DNNs with GNvpro for PDE surrogate modeling applications (Subsection 3.2) and hyperspectral image segmentation (Subsection 3.3). Across these tasks, which involve different loss functions and DNN architectures, solving the reduced problem (2.3) using GNvpro

leads to faster convergence and a more accurate model than solving the full problem (2.2) using a Gauss-Newton-Krylov method or solving the stochastic problem (2.1) using the SGD variant ADAM [32].

3.1. Experimental Setup. In this section, we describe the DNN architectures used in our experiments, define our measure of computational complexity, and describe the optimization strategies we compare. We emphasize that GNvpro does not depend on the architectures and refer to [21] for an overview of possible network designs.

Neural ODEs. In the following experiments, we consider feature extractors given by a neural Ordinary Differential Equation (Neural ODE); see [24, 15, 7]. To this end, we define $F(\mathbf{y}, \boldsymbol{\theta})$ as a numerical approximation of $\mathbf{u}(T)$ that satisfies the initial value problem

$$(3.1) \quad \mathbf{u}(t) = f(\mathbf{u}(t), \mathbf{K}(t), \mathbf{b}(t)) \quad \text{for } t \in (0, T], \quad \mathbf{u}(0) = \sigma(\mathbf{K}_{\text{in}}\mathbf{y} + \mathbf{b}_{\text{in}})$$

with an artificial time $t \in [0, T]$, activation function $\sigma(x) = \tanh(x)$, and weights $\mathbf{K} : [0, T] \rightarrow \mathbb{R}^{N_{\text{out}} \times N_{\text{out}}}$, $\mathbf{b} : [0, T] \rightarrow \mathbb{R}^{N_{\text{out}}}$, $\mathbf{K}_{\text{in}} \in \mathbb{R}^{N_{\text{out}} \times N_{\text{in}}}$, and $\mathbf{b}_{\text{in}} \in \mathbb{R}^{N_{\text{out}}}$. For notational convenience we collectively denote the weights as $\boldsymbol{\theta} = (\mathbf{K}, \mathbf{b}, \mathbf{K}_{\text{in}}, \mathbf{b}_{\text{in}})$.

As shown in [24], the stability of the Neural ODE (3.1) depends both on the choice of weights, which are learned during training, and the layer function f , which is specified prior to training. Here, we use the anti-symmetric layer

$$f(\mathbf{u}, \mathbf{K}, \mathbf{b}) = \sigma \left((\mathbf{K} - \mathbf{K}^{\top} - \gamma \mathbf{I})\mathbf{u} + \mathbf{b} \right),$$

with $\gamma = 10^{-4}$. This design leads to a stable dynamic when \mathbf{K} and \mathbf{b} are constant in time.

To train the Neural ODE, we first discretize its features \mathbf{u} and weights, \mathbf{K} and \mathbf{b} , on the nodes of an equidistant grid of $[0, T]$ with d cells, and then optimize the discretized weights. In our experiments, we use a fourth-order Runge-Kutta scheme. The number of time steps, d , can also be seen as the depth of the network. Hence, our approach is a discretize-optimize method, which has been shown to perform well also in [18, 44].

Optimization and Regularization. We compare GNvpro to the SGD variant ADAM [32] and a standard Gauss-Newton method applied to the full optimization problem (2.2) and the quasi-Newton scheme L-BFGS (implemented following [41]) applied to the VarPro problem (2.3); we call this scheme L-BFGSvpro for brevity. We discuss the hyperparameters of each scheme (e.g., linear solvers, line search methods, learning rates) as well as regularization parameters in the respective sections as they are specific to each task.

To exploit the fact that our learning problems are obtained by discretizing the Neural ODE (3.1), we employ a multilevel training strategy similar to [24, 6, 13]. The idea is to repeatedly solve the learning problem for a shallow-to-deep hierarchy of networks obtained by increasing the depth d in the time discretization. On the first level, we initialize $\boldsymbol{\theta}$, the weights of the feature extractor F , randomly. In our experiments with the full objective functions we initialized \mathbf{W} by solving (2.4) using the methods described in Subsection 2.2 and Subsection 2.3 for the initial network weights. In our examples this has improved the performance over random initialization of \mathbf{W} and also ensures that all schemes start with the same initial guess. After approximately solving the problem on the first level, the final iterate of $\boldsymbol{\theta}$ is prolonged in time using piecewise linear interpolation and used to initialize

the optimization for the network architecture given by discretizing (3.1) with twice as many time steps. This procedure is repeated until the desired depth of the network is reached.

For the Neural ODE weights, the regularization operator \mathbf{B} is a finite-difference, time discretization to promote smooth transitions between layers. For the other weights, we use an identity regularization operator.

Computational Costs. We measure the computational cost of training neural networks with the various optimization schemes in terms of work units, which we define as the sum of the number of forward and backward passes through the network. These forward and backward passes are the most expensive computational steps in training, particularly for deep networks. A forward pass consists of forming the current function value Φ_c in Algorithm 2.1 or a forward application of the Jacobian J_c . A backward pass consists of forming the current gradient $\nabla\Phi_c$ in Algorithm 2.1 or an application of J_c^\top . For simplicity, we ignore the dependency of the cost on the number of time steps, d , which can vary in the multilevel training.

The number of work units per step differs across the optimization methods. For example, each epoch of ADAM requires two work units: one to evaluate the objective function and one to compute its gradient for all examples in the batch (see left column in Algorithm 2.1). Each iteration of L-BFGSvpro requires two work units to compute the objective function and its gradient plus a few additional work units to perform the line search. The iterations of GNvpro require additional $2r$ work units to obtain the low-rank factorization of the approximate Hessian.

3.2. Surrogate Modeling. In this section, we apply GNvpro to two datasets motivated by PDE surrogate modeling with DNNs. One of the key challenges for surrogate modeling consists of capturing the nonlinear features by efficiently manipulating the vast number of input parameters. Creating suitable surrogates that in turn can be used for a range of analysis tasks, such as uncertainty quantification and optimization, requires a necessary level of accuracy. However, when the underlying dynamics is nonlinear and the input to output mapping is nonconvex, the learning process becomes non-trivial.

Our goal is to design a DNN that maps given parameters \mathbf{y} to a set of observables \mathbf{c} , where \mathbf{y} and \mathbf{c} satisfy

$$\mathbf{c} = \mathcal{P}u \quad \text{subject to} \quad \mathcal{A}(u; \mathbf{y}) = 0.$$

The function u is the solution of the PDE and \mathcal{A} is the PDE operator parameterized by \mathbf{y} . The linear operator \mathcal{P} measures the solution u at discrete points in the domain to obtain a set of observables $\mathbf{c} \in \mathbb{R}^{N_{\text{target}}}$.

To train the DNN surrogate, we minimize the least-squares regression loss. For these applications, it is reasonable to assume that the training data contains no noise or errors as it is generated using a fine mesh solver. Hence, an effective surrogate should tightly fit the training data and at the same time be efficient to evaluate. Note that we develop these surrogate models based solely on the parameter-observable pairs, independent of the underlying PDE.

In our experiments, we consider two examples: convection diffusion reaction (CDR), a commonly used PDE which models a variety of physical phenomena, and direct current resistivity (DCR), a inverse conductivity problem using a PDE model for electric potential.

Table 2

Training, validation, and test results for convection diffusion reaction and DC Resistivity. We report mean relative errors \pm standard deviation where the smaller values indicate better fit.

	Training	Validation	Test
Convection Diffusion Reaction			
Full GN	0.0115 ± 0.0055	0.0138 ± 0.0075	0.0142 ± 0.0072
Full SGD	0.0091 ± 0.0045	0.0114 ± 0.0086	0.0116 ± 0.0072
L-BFGSvpro	0.0171 ± 0.0102	0.0219 ± 0.0127	0.0260 ± 0.0187
GNvpro	0.0045 ± 0.0021	0.0057 ± 0.0033	0.0060 ± 0.0032
DC Resistivity			
Full GN	0.3837 ± 0.8384	0.3650 ± 0.6920	0.3517 ± 0.6638
Full SGD	0.2994 ± 0.3652	0.2839 ± 0.2776	0.2904 ± 0.3256
L-BFGSvpro	0.0786 ± 0.1878	0.0763 ± 0.1887	0.0747 ± 0.1625
GNvpro	0.0198 ± 0.0311	0.0191 ± 0.0258	0.0199 ± 0.0322

Both examples are summarized below and fully described in [Appendix A](#). The CDR equation has inspired mathematical models for studying problems in many fields, such as subsurface flows [9, 37], atmospheric dispersion modeling [1], semi-conductor physics [28], chemical vapor deposition [17], biomedical engineering [39, 16], population dynamics [61, 3], combustion [38], and wildfire spread [22]. In the CDR example we consider, the inputs $\mathbf{y} \in \mathbb{R}^{55}$ which parameterizes the reaction function and the targets $\mathbf{c} \in \mathbb{R}^{72}$ which are observations of the state u at 6 fixed spatial locations and 12 instances of time. The data set consists of 800 pairs of parameters (\mathbf{y}, \mathbf{c}) generated by repeatedly solving the PDE.

Direct Current Resistivity (DCR) seeks detect an object from indirect noisy measurements [54, 14]. The mathematical formulation is general and a similar instance of this problem also arises in modeling porous media flow with Darcy's Law [8]. We illustrate surrogate modeling where the inputs $\mathbf{y} \in \mathbb{R}^3$ parameterize the depth, volume, and orientation of an ellipsoidal conductivity model and the targets $\mathbf{c} \in \mathbb{R}^{882}$ correspond to the observed electric potential differences. We generate 6000 samples of parameters and observables (\mathbf{y}, \mathbf{c}) .

For both examples, we train the Neural ODE model [\(3.1\)](#) with a width of $N_{\text{out}} = 8$ and $N_{\text{out}} = 16$ for the CDR and DCR examples, respectively, and a final time of $T = 4$. Our multi-level approach consists of three steps whose respective number of time steps is 2, 4, and 8. For GNvpro, we limit the rank of the Krylov subspace to $r_{\text{max}} = 20$ and use a relative residual tolerance of 10^{-2} . For SGD, we use the final depth of the network with a batch size of 2 and a learning rate of 10^{-3} . For all optimization strategies, we use Tikhonov regularization with $\alpha_1 = \alpha_2 = 10^{-10}$ to prioritize fitting.

We report the CDR and DCR numerical results in [Table 2](#). GNvpro produces the most accurate surrogate models for both the CDR and DCR experiments in [Table 2](#). In the DCR experiment, GNvpro reduces the data fit by an additional order of magnitude compared to the Gauss-Newton and ADAM methods applied to the full objective function and also outperforms L-BFGSvpro. As revealed by the convergence plots in [Figure 2](#), GNvarpro achieves this level of accuracy in fewer work units.

Strikingly, the GNvpro solution also generalizes best, that is, it leads to the lowest valida-

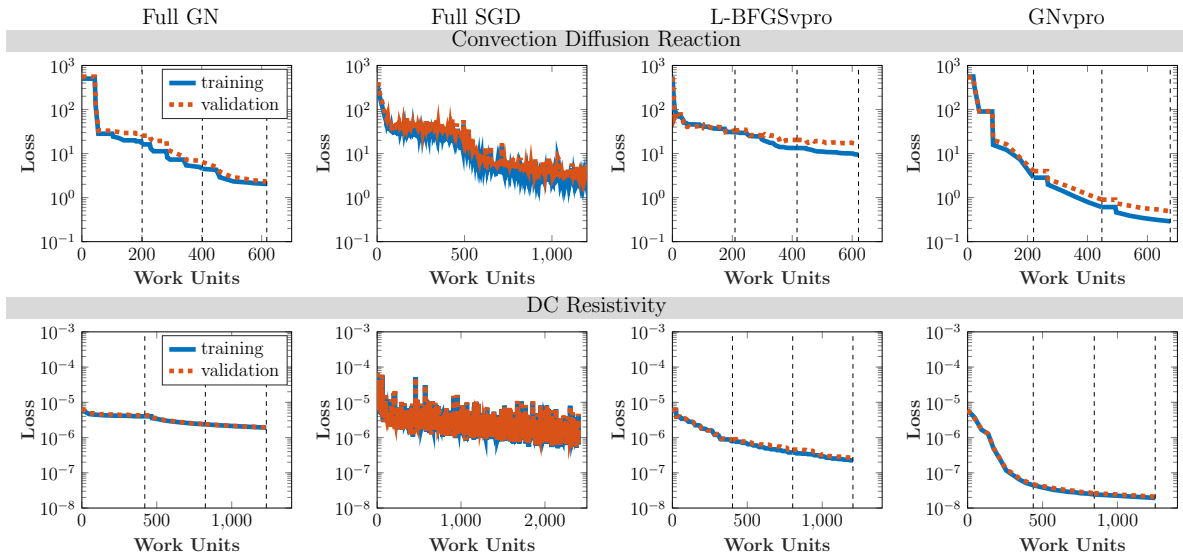


Figure 2. We plot the convergence of the loss in the CDR and DCR experiments for the various optimization strategies. The weights of the Neural ODE are prolonged twice, indicated by the vertical dashed lines in each plot. GNvpro outperforms all other approaches and achieves the best fit in the fewest number of work units whereas L-BFGSvpro achieves a moderate accuracy and the Gauss-Newton and SGD schemes fail to achieve a sufficient accuracy.

tion and test errors in [Table 2](#) and most efficient reduction of the validation loss in [Figure 2](#). Generalization is particularly significant in scientific applications to ensure the reliability of surrogate models.

To further support our numerical findings, we visualize the prediction obtained from the DNN surrogates for the CDR and DCR experiments in [Figure 3](#). Each image in [Figure 3](#) contains all of the observables and the DNN approximations to the observables as columns of the matrix thereby providing a global visualization of the performance of our surrogate models. The width of each image is the total number of samples that we partition into training, validation, and test sets. The difference images are the most illuminating about the quality of approximation. We see that training with GNvpro produces difference images with values closest to zero, supporting our numerical findings in [Table 2](#).

For the DCR experiments, we can gain additional insight by visualizing the output $\mathbf{c} \in \mathbb{R}^{882}$ as two 21×21 images for a few randomly chosen examples in [Figure 4](#). As expected from the small loss values, GNvpro best captures the pattern of the observed, true data for both the training and validation examples. L-BFGSvpro and Gauss-Newton retain some resemblance to the true data, including some of the ellipsoidal structure in the left blocks of each image. In comparison, the SGD prediction does not capture the structure in the images, further demonstrating the competitiveness of GNvpro.

Together, these numerical results and visualizations demonstrate that training with GNvpro provides a more reliable PDE surrogate model that generalizes well and outperforms SGD in terms of both convergence speed and accuracy.

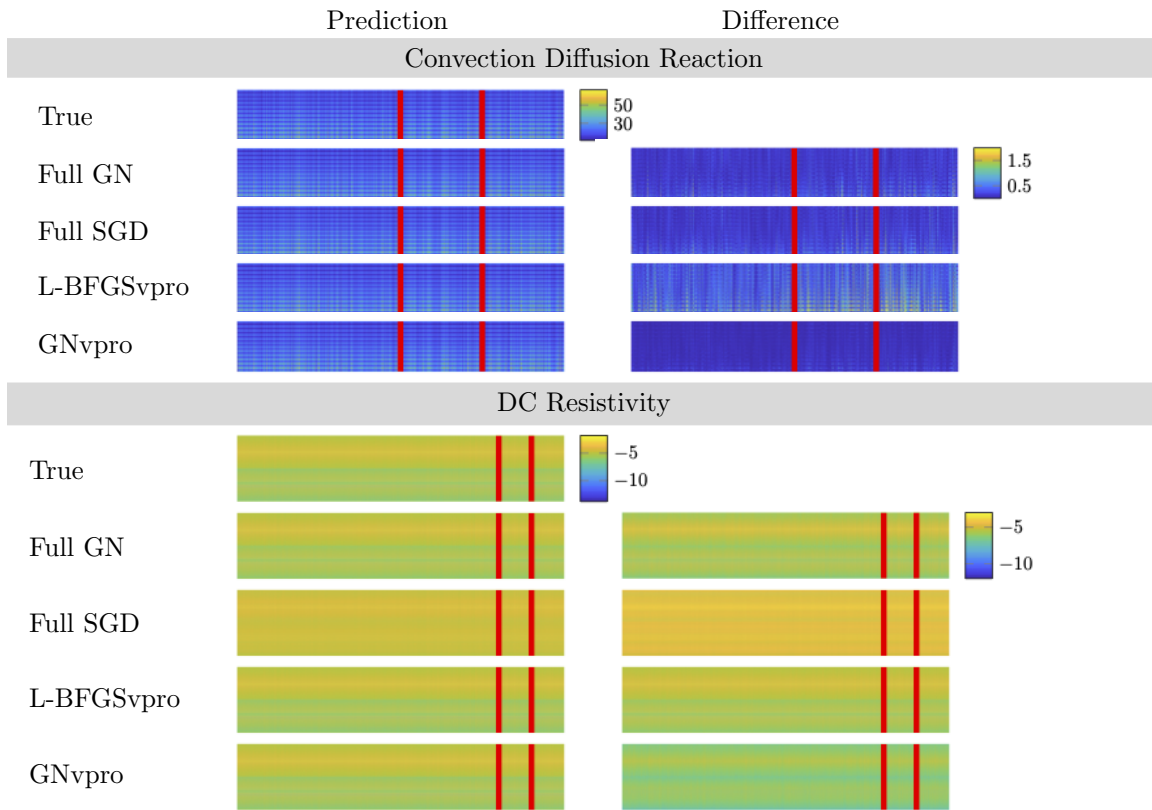


Figure 3. Global visualization of DNN surrogate model approximations for CDR and DCR data. In the left images, each column of each image represents the output of the trained Neural ODE for different samples. In the right images, we display the absolute difference between the predicted outputs and the true data. To improve visibility of the DCR data, the absolute value of the data and their difference is used and intensities are scaled logarithmically. The red lines divide the data into training, validation, and test sets, left-to-right. From the difference images and numerical results in Table 2, the GNvpro is the most similar to the true, observed data.

3.3. Indian Pines. We demonstrate the ability of GNvpro to efficiently solve multinomial regression problems using the Indian Pine dataset [2], a hyperspectral image dataset containing of electromagnetic images of agricultural crops. The image data has 145×145 pixels and 220 spectral reflectance bands. The goal is to partition a hyperspectral image based on the crop or material in the given location. The 16 different material types are provided in Figure 5. We consider each pixel of data to be an input feature vector of length 220. We randomly split the pixels into training, validation, and test datasets. Achieving generalization of the DNN model is also complicated by the large variations of the number of pixels among the different crops. We visualize this class imbalance in Figure 5.

We train the Neural ODE model (3.1) with a width of $N_{\text{out}} = 32$ and a final time of $T = 4$. Our multi-level approach consists of three steps whose respective number of time steps is 4, 8, and 16. For GNvpro, we limit the rank of the Krylov subspace to $r_{\text{max}} = 50$ and use a relative residual tolerance of 10^{-2} . For SGD, we use the final depth of the network and train with a

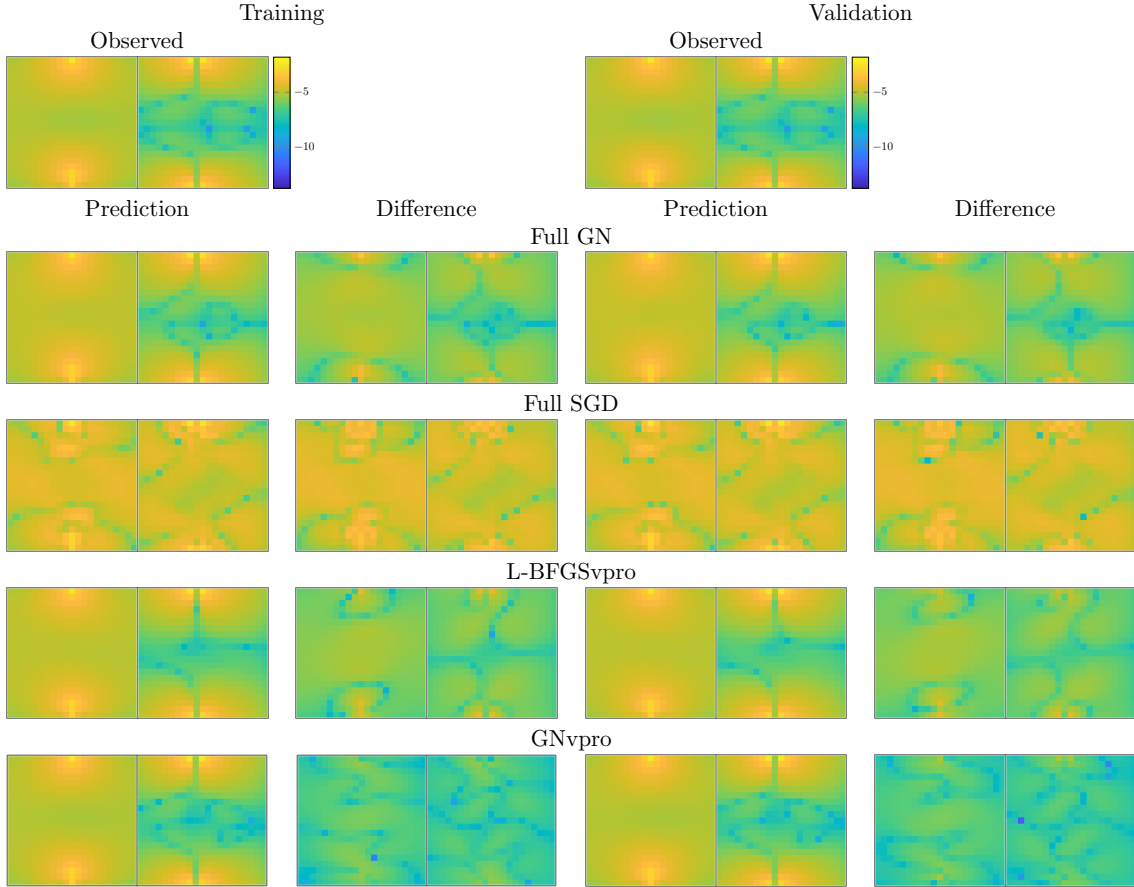


Figure 4. Local DCR surrogate model results. The left two columns show an example from the training set as well as absolute errors of the prediction. The right two columns show an example from the validation set. To improve visibility, we show the absolute value of the data and scale all axes logarithmically. Each image contains two 21×21 blocks representing the difference in potential on the subsurface in the x -direction and y -direction, respectively. We notice that training the full models results in noisy approximations to the training and validation examples.

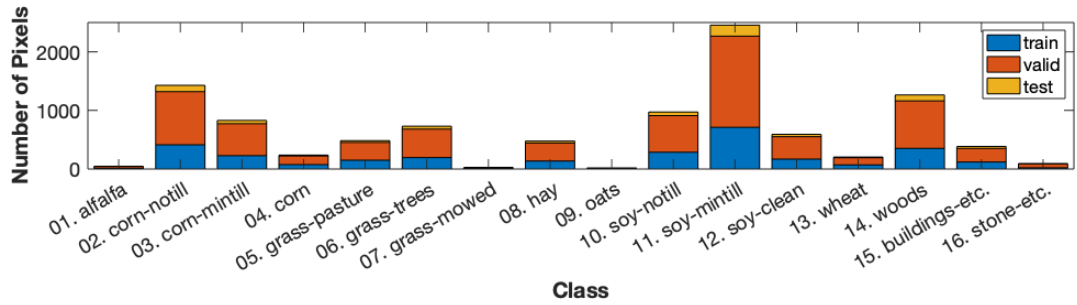


Figure 5. Distribution of Indian Pines data. Each bar represents the total number of pixels belonging to each of the 16 classes. The bars are split into training (blue) and validation (pixels). The smallest classes (1, 4, 7, 9, 13, 16) are split to have 10 validation pixels, the remaining classes have $\lfloor 5000/16 \rfloor = 312$ training pixels each.

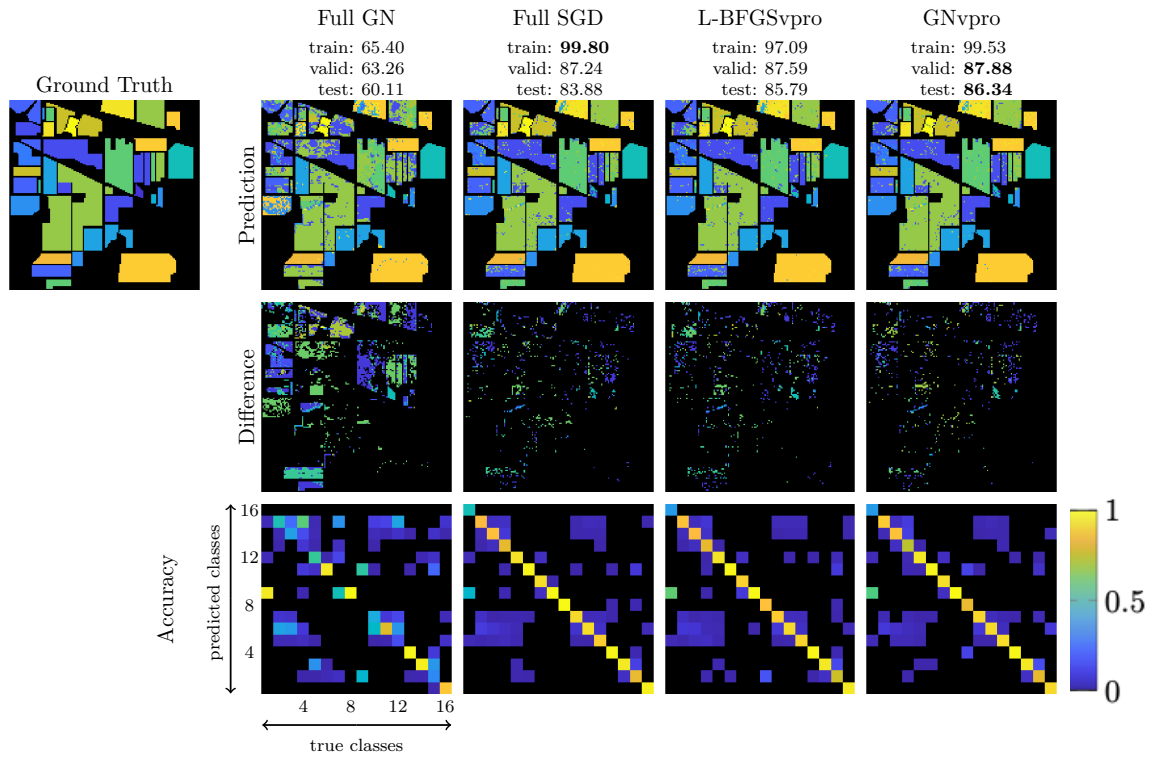


Figure 6. Comparison of optimization schemes for segmenting the Indian Pines hyperspectral dataset; each column corresponding to Gauss-Newton, GNvpro, SGD, and L-BFGSvpro, respectively. The “Prediction” row contains the prediction maps where each color corresponds to a different class. We use the network that produced the highest validation accuracy to create the prediction. The “Difference” row contains the absolute difference between the prediction and the ground truth. The “Accuracy” row contains confusion matrices to visualize the accuracy per class. Each (i, j) -entry of the confusion matrices is the ratio of the number of times a pixel was classified as class i that truly belonged to class j . Each column is normalized by the total number of pixels belonging to class j from the true labeling, so the sum of every column is equal to 1. Thus, each (i, j) -entry can be thought of as the probability that a predicted class i belongs to class j . We want to see high probabilities along the diagonal entries. We plot the convergence of the accuracy and the loss for each optimization method for training and validation data. Note that we ran SGD for twice as many work units as the other methods and kept the weights corresponding to the highest validation accuracy (black dot).

batch size of 32 and a learning rate of 10^{-3} . For all optimization strategies, we use Tikhonov regularization with $\alpha_1 = \alpha_2 = 10^{-3}$. We display the prediction results in Figure 6 and plot the convergence histories in Figure 7.

In Figure 6, we see that GNvpro outperforms training without VarPro in terms of convergence of the accuracy and loss. In fact, from the confusion matrix, we see the full Gauss-Newton optimization did not correctly predict any pixels belonging to material 1, 7, and 9. These groups contained the fewest number of pixels (Figure 5) and thus are challenging to classify correctly. In its inner loop (2.4), GNvpro solves for a classification matrix based on all pixels, including those belonging to the smallest classes, resulting in better classification overall. We note our results could be further improved by, e.g., taking spatial information

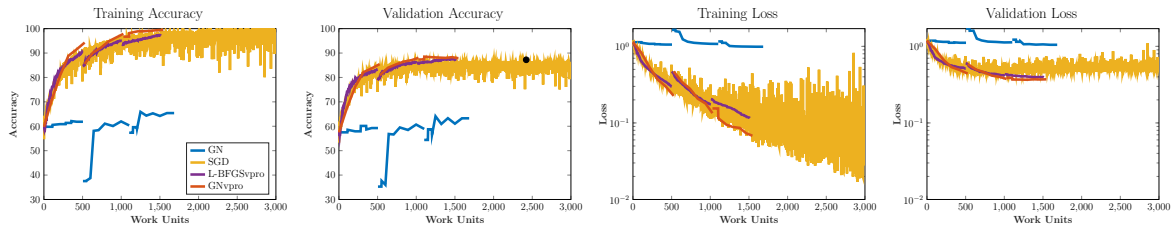


Figure 7. We plot the convergence of the accuracy and the loss for each optimization method for training and validation data. Note that we ran SGD for twice as many work units as the other methods and kept the weights corresponding to the highest validation accuracy (black dot).

into account; see, for instance, [51].

In this experiment, GNvpro achieves the best solution, in terms of validation, test accuracy, and computational costs; for example, it uses only 60% the number of work units that we used for ADAM and improves the test accuracy by more than 2%. The training efficiency can be translated to faster runtimes by exploiting the straightforward parallelism of GNvpro. In addition, the overhead of solving for the optimal linear transformation is minimal, taking only 6.4% of the total training time. We highlight the improved generalization of VarPro training, since a popular belief is that SAA methods overfit more easily. VarPro improves our ability to reduce the loss function, which offers new opportunities to improve generalization by well-crafted direct regularization in contrast to the implicit generalization provided by SGD. Through this image segmentation problem with cross-entropy loss, we demonstrate that both GNvpro and L-BFGSvpro converge faster and yield more solutions that generalizes better compared to Gauss-Newton without VarPro and the SGD variant ADAM.

4. Conclusions. We present GNvpro, a highly effective Gauss-Newton implementation of variable projection (VarPro) that accelerates the training of deep neural networks (DNNs). Our method extends the reach of VarPro beyond least-squares loss functions to cross-entropy losses to support classification tasks. As the projection in the non-quadratic case has no closed-form solution, we derive a Newton-Krylov trust region method to efficiently solve the resulting smooth, convex optimization problem. Due to our efficient implementation the computational cost of DNN training is dominated by forward and backward propagations through the feature extractor, and the computational costs of the projection step are insignificant in practice. A key step in the derivation of GNvpro is the computation of matrix-vector products with the Jacobian of the reduced DNN model for which we use implicit differentiation and re-use matrix factorizations from the projection step.

The key motivation to use VarPro is to exploit the separable structure of most common DNN architectures to improve the convergence of the training scheme. The mechanics of VarPro are similar to those of block coordinate descent approaches (e.g., the recent DNN training algorithms in [45, 12]). Added challenges in VarPro are the higher accuracy needed for the inner problem and the slightly more involved derivations of Jacobians for the outer problem when using Gauss-Newton-type approaches. A key contribution of our paper is the derivation of efficient algorithms and their implementations that limit the computational costs of those parts, rendering the computational costs of GNvpro comparable to block coordinate

descent. A crucial advantage added by GNvpro is its ability to account for the expected coupling between \mathbf{W} and $\boldsymbol{\theta}$ and therefore may be more efficient (for some evidence, see the imaging examples in [10]).

To demonstrate the applicability of GNvpro, our numerical experiments vary the DNN architecture to accomplish two learning tasks, namely segmentation and surrogate modeling. We provide numerical experiments for multilayer perceptron (see Figure 1) and Neural ODEs, different loss functions (linear regression, logistic regression, multinomial regression), and optimization methods (Gauss-Newton, BFGS, ADAM). Across all of these experiments, GNvpro trains the networks more efficiently, i.e., it achieves a lower training loss for a given number of work units. Furthermore, the high validation accuracy indicates that the trained DNNs also generalize well. We note that in addition to fewer work units, the straightforward parallelism offered by SAA methods can dramatically reduce the computational time of DNN training.

Our numerical experiments suggests that GNvpro has a few traits that make it particularly useful for PDE surrogate modeling. Most importantly, VarPro improves the accuracy of the learned parameter-to-observable map by an order of magnitude compared to both SAA and SGD methods that do not exploit the structure of the architecture. As in this application the data is not corrupted by noise, this accuracy is meaningful for practical applications that rely on computationally-efficient surrogate models of complex physical systems. VarPro may also provide new avenues for solving other learning problems for which existing methods fail to reduce the loss function sufficiently; for example, scientific applications such as solving PDEs using neural networks.

Our primary reason to use an SAA method is to avoid overfitting when solving the inner optimization problem (2.4). As SAA methods generally use larger batch sizes compared to stochastic approximation methods such as SGD, the risk is reduced. Even though the SAA methods perform well in our examples, exploring the use of VarPro in SGD-type methods is an interesting open question.

For future work, we will investigate the benefits of GNvpro across an even wider range of learning problems. To this end, we make our prototype implementation freely available as part of the `Meganet.m` package, a public MATLAB neural network repository also used in [24, 52]. To further its reach, we also plan to implement GNvpro in other machine learning frameworks such as TensorFlow and pyTorch.

Acknowledgments. We thank Eldad Haber for introducing us to Variable Projection and many fruitful discussions. Any subjective views or opinions that might be expressed in the paper do not necessarily represent the views of the U.S. Department of Energy or the United States Government. Sandia National Laboratories is a multimission laboratory managed and operated by National Technology and Engineering Solutions of Sandia LLC, a wholly owned subsidiary of Honeywell International, Inc., for the U.S. Department of Energy's National Nuclear Security Administration under contract DE- NA-0003525. SAND2020-7339 O.

REFERENCES

- [1] ÁDÁM LEELOSSY, F. M. JR., F. IZSÁK, ÁGNES HAVASI, I. LAGZI, AND R. MÉSZÁROS, *Dispersion modeling of air pollutants in the atmosphere: a review*, Central European Journal of Geosciences, 6 (2014), pp. 257–278.

- [2] M. F. BAUMGARDNER, L. L. BIEHL, AND D. A. LANDGREBE, *220 band aviris hyperspectral image data set: June 12, 1992 indian pine test site 3*, Sep 2015, <https://doi.org/doi:10.4231/R7RX991C>, <https://purr.psu.edu/publications/1947/1>.
- [3] M. BAURMANNA, T. GROSS, AND U. FEUDEL, *Instabilities in spatially extended predator-prey systems: spatio-temporal patterns in the neighborhood of turinghopf bifurcations*, Journal of Theoretical Biology, 245 (2007), pp. 220–229.
- [4] R. BOLLAPRAGADA, R. H. BYRD, AND J. NOCEDAL, *Exact and inexact subsampled newton methods for optimization*, IMA Journal of Numerical Analysis, 39 (2018), pp. 545–578, <https://doi.org/10.1093/imanum/dry009>, <http://dx.doi.org/10.1093/imanum/dry009>.
- [5] L. BOTTOU, F. E. CURTIS, AND J. NOCEDAL, *Optimization methods for large-scale machine learning*, SIAM Review, 60 (2018), pp. 223–311.
- [6] B. CHANG, L. MENG, E. HABER, F. TUNG, AND D. BEGERT, *Multi-level Residual Networks from Dynamical Systems View*, arXiv.org, (2017), <https://arxiv.org/abs/1710.10348v2>.
- [7] T. Q. CHEN, Y. RUBANOVA, J. BETTENCOURT, AND D. DUVEAUD, *Neural Ordinary Differential Equations*, in NeurIPS, June 2018.
- [8] Z. CHEN, G. HUAN, AND Y. MA, *Computational Methods for Multiphase Flows in Porous Media*, SIAM, Philadelphia, 2010.
- [9] E.-V. C. CHOQUET AND ÉLOÏSE COMTE, *Optimal control for a groundwater pollution ruled by a convection-diffusion-reaction problem*, Journal of Optimization Theory and Applications, (2017).
- [10] J. CHUNG, E. HABER, AND J. NAGY, *Numerical methods for coupled super-resolution*, Inverse Problems, 22 (2006), pp. 1261–1272.
- [11] G. CYBENKO, *Approximations by superpositions of a sigmoidal function*, Mathematics of Control, Signals, and Systems, 2 (1989), pp. 303–314.
- [12] E. C. CYR, M. A. GULIAN, R. G. PATEL, M. PEREGO, AND N. A. TRASK, *Robust training and initialization of deep neural networks: An adaptive basis viewpoint*, Proceedings of Machine Learning Research vol. 107 (2020), pp. 1–26.
- [13] E. C. CYR, S. GÜNTHER, AND J. B. SCHRODER, *Multilevel initialization for layer-parallel deep neural network training*, arXiv preprint arXiv:1912.08974, (2019).
- [14] A. DEY AND H. MORRISON, *Resistivity modeling for arbitrarily shaped three dimensional structures*, Geophysics, 44 (1979), pp. 753–780.
- [15] W. E, *A Proposal on Machine Learning via Dynamical Systems*, Comm. Math. Statist., 5 (2017), pp. 1–11, <https://doi.org/10.1007/s40304-017-0103-z>, <http://link.springer.com/10.1007/s40304-017-0103-z>.
- [16] S. FERREIRA, M. MARTINS, AND M. VILELA, *Reaction-diffusion model for the growth of avascular tumor*, Physics Review, 65 (2002).
- [17] J. GEISER, *Multiscale modeling of chemical vapor deposition (cvd) apparatus: Simulations and approximations*, Polymers, 5 (2013), pp. 142–160.
- [18] A. GHOLAMI, K. KEUTZER, AND G. BIROS, *ANODE: Unconditionally Accurate Memory-Efficient Gradients for Neural ODEs*, arXiv.org, (2019), <https://arxiv.org/abs/1902.10298v1>.
- [19] G. GOLUB AND V. PEREYRA, *The differentiation of pseudo-inverses and nonlinear least squares problems whose variables separate*, SIAM Journal on Numerical Analysis, 10 (1973), pp. 413–432.
- [20] G. GOLUB AND V. PEREYRA, *Separable nonlinear least squares: the variable projection method and its applications*, Inverse Problems, 19 (2003), pp. R1–R26.
- [21] I. GOODFELLOW, Y. BENGIO, AND A. COURVILLE, *Deep Learning*, MIT Press, Nov. 2016.
- [22] P. GRASSO AND M. S. INNOCENTE, *Advances in Forest Fire Research: A two-dimensional reaction-advection-diffusion model of the spread of fire in wildlands*, Imprensa da Universidade de Coimbra, 2018.
- [23] E. HABER, *Computational methods in geophysical electromagnetics*, Mathematics in Industry (Philadelphia), Society for Industrial and Applied Mathematics (SIAM), Philadelphia, PA, 2015.
- [24] E. HABER AND L. RUTHOTTO, *Stable architectures for deep neural networks*, Inverse Probl., 34 (2017), p. 014004, <https://arxiv.org/abs/1705.03341>.
- [25] J. HAN, A. JENTZEN, AND E. WEINAN, *Solving high-dimensional partial differential equations using deep learning*, Proceedings of the National Academy of Sciences, 115 (2018), pp. 8505–8510.
- [26] K. HE, X. ZHANG, S. REN, AND J. SUN, *Deep residual learning for image recognition*, in Proceedings of the IEEE Conference on Computer Vision and Pattern Recognition, 2016, pp. 770–778.

- [27] G. HINTON, L. DENG, D. YU, G. E. DAHL, A. MOHAMED, N. JAITLEY, A. SENIOR, V. VANHOUCKE, P. NGUYEN, T. N. SAINATH, AND B. KINGSBURY, *Deep neural networks for acoustic modeling in speech recognition: The shared views of four research groups*, IEEE Signal Processing Magazine, 29 (2012), pp. 82–97.
- [28] A. JUNGEL, ed., *Transport Equations for Semiconductors*, Lecture Notes in Physics, Springer, 2013.
- [29] L. KAUFMAN, *A variable projection method for solving separable nonlinear least squares problems*, BIT, (1975), pp. 49–57.
- [30] C. T. KELLEY, *Iterative Methods for Optimization*, SIAM, Philadelphia, Jan. 1999.
- [31] S. KIM, R. PASUPATHY, AND S. HENDERSON, *A Guide to Sample Average Approximation*, vol. 216, Springer, 01 2015, pp. 207–243, https://doi.org/10.1007/978-1-4939-1384-8_8.
- [32] D. P. KINGMA AND J. BA, *Adam: A method for stochastic optimization*, arXiv preprint arXiv:1412.6980, (2014).
- [33] A. J. KLEYWEGT, A. SHAPIRO, AND T. HOMEM-DE MELLO, *The sample average approximation method for stochastic discrete optimization*, SIAM Journal on Optimization, 12 (2002), pp. 479–502, <https://doi.org/10.1137/S1052623499363220>, <https://doi.org/10.1137/S1052623499363220>, <https://arxiv.org/abs/https://doi.org/10.1137/S1052623499363220>.
- [34] A. KRIZHEVSKY, I. SUTSKEVER, AND G. E. HINTON, *Imagenet classification with deep convolutional neural networks*, NIPS, (2012).
- [35] Y. LECUN, B. BOSER, J. S. DENKER, D. HENDERSON, R. E. HOWARD, W. HUBBARD, AND L. D. JACKEL, *Handwritten digit recognition with a back-propagation network*, Advances in Neural Information Processing Systems, 2 (1990).
- [36] H. LI, Z. XU, G. TAYLOR, C. STUDER, AND T. GOLDSTEIN, *Visualizing the loss landscape of neural networks*, in 32nd Conference on Neural Information Processing Systems, 2018.
- [37] L. LI AND Z. YIN, *Numerical simulation of groundwater pollution problems based on convection diffusion equation*, American Journal of Computational Mathematics, 7 (2017), pp. 350–370.
- [38] M. LUCCHESI, H. H. ALZAHRANI, C. SAFTA, AND O. M. KNIO, *A hybrid, non-split, stiff/rkc, solver for advectiondiffusionreaction equations and its application to low-mach number combustion*, Combustion Theory and Modelling, (2019).
- [39] A. MADZVAMUSE, R. D. K. THOMAS, P. K. MAINI, AND A. J. WATHEN, *A numerical approach to the study of spatial pattern formation in the ligaments of arcoid bivalves*, Bulletin of Mathematical Biology, 64 (2002), pp. 501–530.
- [40] A. NEMIROVSKI, A. JUDITSKY, G. LAN, AND A. SHAPIRO, *Robust stochastic approximation approach to stochastic programming*, SIAM Journal on Optimization, 19 (2009), pp. 1574–1609, <https://doi.org/10.1137/070704277>, <https://doi.org/10.1137/070704277>, <https://arxiv.org/abs/https://doi.org/10.1137/070704277>.
- [41] J. NOCEDAL AND S. J. WRIGHT, *Numerical Optimization*, Springer, second edition ed., 2006.
- [42] D. P. O'LEARY AND B. W. RUST, *Variable projection for nonlinear least squares problems*, Computational Optimization and Applications. An International Journal, 54 (2013), pp. 579–593.
- [43] T. O'LEARY-ROSEBERRY, N. ALGER, AND O. GHATTAS, *Inexact Newton Methods for Stochastic Non-Convex Optimization with Applications to Neural Network Training*, arXiv, (2019), <https://arxiv.org/abs/1905.06738>.
- [44] D. ONKEN AND L. RUTHOTTO, *Discretize-Optimize vs. Optimize-Discretize for Time-Series Regression and Continuous Normalizing Flows*, arXiv.org, (2020), <https://arxiv.org/abs/2005.13420v1>.
- [45] R. G. PATEL, N. A. TRASK, M. A. GULIAN, AND E. C. CYR, *A block coordinate descent optimizer for classification problems exploiting convexity*, arXiv preprint arXiv:2006.10123, (2020).
- [46] V. PEREYRA, G. SCHERER, AND F. WONG, *Variable projections neural network training*, Mathematics and Computers in Simulation, 73 (2006), pp. 231–243.
- [47] K. B. PETERSEN AND M. S. PEDERSEN, *The matrix cookbook*, Oct. 2008, <http://www2.imm.dtu.dk/pubdb/p.php?3274>. Version 20081110.
- [48] M. RAISSI, P. PERDIKARIS, AND G. KARNIADAKIS, *Physics-informed neural networks: A deep learning framework for solving forward and inverse problems involving nonlinear partial differential equations*, Journal of Computational Physics, Elsevier, 378 (2019), pp. 686–707.
- [49] H. ROBBINS AND S. MONRO, *A Stochastic Approximation Method*, The annals of mathematical statistics, 22 (1951), pp. 400–407.

- [50] O. RONNEBERGER, P. FISCHER, AND T. BROX, *U-net: Convolutional networks for biomedical image segmentation*, 2015, <https://arxiv.org/abs/1505.04597>.
- [51] S. K. ROY, G. KRISHNA, S. R. DUBEY, AND B. B. CHAUDHURI, *Hybridsn: Exploring 3d-2d CNN feature hierarchy for hyperspectral image classification*, CoRR, abs/1902.06701 (2019), <http://arxiv.org/abs/1902.06701>, <https://arxiv.org/abs/1902.06701>.
- [52] L. RUTHOTTO AND E. HABER, *Deep neural networks motivated by partial differential equations*, Journal of Mathematical Imaging and Vision, 62 (2019), p. 352364, <https://doi.org/10.1007/s10851-019-00903-1>, <http://dx.doi.org/10.1007/s10851-019-00903-1>.
- [53] Y. SAAD, *Iterative Methods for Sparse Linear Systems*, Second Edition, SIAM, Philadelphia, Apr. 2003.
- [54] K. SEIDEL AND G. LANGE, *Direct Current Resistivity Methods*, Springer Berlin Heidelberg, Berlin, Heidelberg, 2007, pp. 205–237, https://doi.org/10.1007/978-3-540-74671-3_8, https://doi.org/10.1007/978-3-540-74671-3_8.
- [55] J. SIRIGNANO, K. SPILIOPOULOS, AND 2018, *DGM: A deep learning algorithm for solving partial differential equations*, Computers Chem Engn., 375 (2018), pp. 1339–1364.
- [56] J. SJÖBERG AND M. VIBERG, *Separable non-linear least-squares minimization-possible improvements for neural net fitting*, in Neural Networks for Signal Processing VII. Proceedings of the 1997 IEEE Signal Processing Society Workshop, 1997.
- [57] R. K. TRIPATHY AND I. BILIONIS, *Deep UQ: Learning deep neural network surrogate models for high dimensional uncertainty quantification*, Journal of Computational Physics, 375 (2018), pp. 565–588.
- [58] E. WEINAN AND B. YU, *The deep Ritz method: a deep learning-based numerical algorithm for solving variational problems*, Communications in Mathematics and Statistics, 6 (2018), pp. 1–12.
- [59] P. XU, F. ROOSTA, AND M. W. MAHONEY, *Second-order optimization for non-convex machine learning: an empirical study*, Proceedings of the 2020 SIAM International Conference on Data Mining, (2020), pp. 199–207, <https://doi.org/10.1137/1.9781611976236.23>, <http://dx.doi.org/10.1137/1.9781611976236.23>.
- [60] Z. YAO, A. GHOLAMI, S. SHEN, K. KEUTZER, AND M. W. MAHONEY, *Adahessian: An adaptive second order optimizer for machine learning*, 2020, <https://arxiv.org/abs/2006.00719>.
- [61] F. YI, J. WEI, AND J. SHI, *Bifurcation and spatiotemporal patterns in a homogeneous diffusive predator-prey system*, Journal of Differential Equations, 246 (2009), p. 1944197.

Appendix A. Data Generation for Regression Examples.

To supplement Subsection 3.2, we provide details about the PDE models.

Convection Diffusion Reaction (CDR). We consider the CDR equation defined on the time interval $[0, 0.5]$ and spatial domain $\Omega = (0, 1)^2$ with a zero initial condition and homogeneous Neumann conditions on the boundary $\partial\Omega = [0, 1]^2 \setminus \Omega$, i.e.

$$\begin{aligned} \frac{\partial u}{\partial t} &= \nabla \cdot (D \nabla u) - \mathbf{v} \cdot \nabla u + f + \mathbf{y}^T \mathbf{r}(u) && \text{on } \Omega \times (0, 0.5] \\ D \nabla u \cdot \mathbf{n} &= 0 && \text{on } \partial\Omega \times (0, 0.5] \\ u &= 0 && \text{on } \Omega \cup \partial\Omega \times \{0\} \end{aligned}$$

where $u : [0, 1]^2 \times [0, 0.5] \rightarrow \mathbb{R}$ is the state variable (e.g., concentration), $D = 0.5$ is the diffusion coefficient, $\mathbf{v} : (0, 1)^2 \rightarrow \mathbb{R}^2$ is the (stationary) velocity field given by

$$\mathbf{v}(x_1, x_2) = (4.5(1 + 0.8 \sin(2\pi x_1)), 5.5(0.5 - x_2)),$$

and $f : [0, 1]^2 \times [0, 0.5] \rightarrow \mathbb{R}$ is the source term given by

$$\begin{aligned} f(x_1, x_2, t) &= 1000(1.0 + 0.3 \cos(2\pi t)) \exp(-200((x_1 - 0.2)^2 + (x_2 - 0.2)^2)) \\ &\quad + 800(1.2 + 0.4 \sin(4\pi t)) \exp(-200((x_1 - 0.6)^2 + (x_2 - 0.8)^2)) \\ &\quad + 900(0.9 + 0.2 \sin(6\pi t)) \exp(-200((x_1 - 0.3)^2 + (x_2 - 0.6)^2)). \end{aligned}$$

The velocity field \mathbf{v} and centers of the Gaussian source locations are shown in the left panel of Figure 8. The reaction term $\mathbf{y}^T \mathbf{r}(u)$ (a nonlinear function of the state u) is the inner product of the parameter vector $\mathbf{y} \in \mathbb{R}^{55}$ and

$$\mathbf{r}(u) = \bar{r} (r_{1,2}(u), r_{1,3}(u), \dots, r_{1,11}(u), r_{2,3}(u), r_{2,4}(u), \dots, r_{2,11}(u), r_{3,4}(u), \dots, r_{10,11}(u))^T$$

which combines the reaction functions

$$r_{i,j}(u) = \left(\frac{C \exp \left(\ln (C^{-2}) \frac{u-u_i}{u_j-u_i} \right)}{1 + C \exp \left(\ln (C^{-2}) \frac{u-u_i}{u_j-u_i} \right)} \right),$$

where $C = \frac{10^{-3}}{1-10^{-3}}$ and $u_i = 5 + 6(i-1)$, $i = 1, 2, \dots, 11$, and the spatially heterogeneous scaling field

$$\bar{r}(x_1, x_2) = 500 (0.8 + 0.2 \sin(2\pi x_1) \cos(2\pi x_2) + x_2).$$

The reaction functions $\{r_{i,j}\}$ are a set of 55 sigmoid functions which activate (begin taking values $\gg 0$) and saturate (approach their vertical asymptote 1) for different values of u , i.e. they model reactions which occur over various concentration ranges. The center panel of Figure 8 shows each $r_{i,j}$ plotted as a function of u .

The state u is initially zero, but increases through the time dependent forcing f , is advected toward $(1.0, 0.5)$ by the velocity field \mathbf{v} , and undergoes diffusion and spatially heterogeneous reaction. The right panel of Figure 8 displays a typical realization of the state u at the final time $t = 0.5$.

We solve the PDE using linear finite elements on a rectangular mesh containing 151 nodes in each spatial dimension, and 51 steps using backward Euler on a uniform time grid.

The reaction function coefficients (the input data) $\mathbf{y} \in \mathbb{R}^{55}$ are generated by sampling each component of \mathbf{y} independently from a uniform distribution on $[0, 1]$ and subsequently normalizing by the sum of components. The target data \mathbf{c} is generated by evaluating the solution $u(x_1, x_2, t)$ at six spatial locations (indicated by the circles overlaying the plot in the right panel of Figure 8) for each of the final twelve time steps, i.e. at times $t = 0.39 + 0.01k$, $k = 0, 1, \dots, 11$.

Direction Current Resistivity (DCR). The PDE modeling the electric potential in the DCR example is given by Poisson's equation on the spatial domain $\Omega = (0, 2) \times (0, 2) \times (0, 1)$ with homogenous Neumann conditions on $\partial\Omega = [0, 2] \times [0, 2] \times [0, 1] \setminus \Omega$, i.e.

$$\begin{aligned} -\nabla \cdot (m(\cdot, \mathbf{y}) \nabla u) &= q && \text{on } \Omega \\ \nabla u \cdot \mathbf{n} &= 0 && \text{on } \partial\Omega \end{aligned}$$

where $u : \Omega \rightarrow \mathbb{R}$ is the state variable (e.g., the electric potential) and $q : \Omega \rightarrow \mathbb{R}$ is a source (e.g., a dipole) visualized in Figure 9.

The model or control variable $m : \Omega \times \mathbb{R}^{N_{\text{in}}} \rightarrow \mathbb{R}_+$ (e.g., conductivity), parameterized by $\mathbf{y} \in \mathbb{R}^3$, is given by

$$m(\mathbf{x}; \mathbf{y}) = \exp \left(10 \exp \left(-\frac{1}{y_2^2} \left(\left\| \text{diag}(\sqrt{2}, 1) \mathbf{Q}(y_3) \begin{pmatrix} x_1 - 1 \\ x_2 - 1 \end{pmatrix} \right\|^2 + (x_3 - y_1)^2 \right) \right) \right),$$

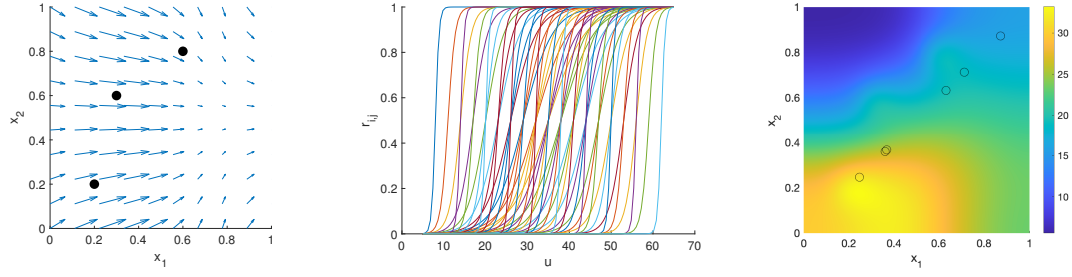


Figure 8. Visualizing the generation for the Convection Diffusion Reaction dataset. Left: velocity field \mathbf{v} with direction denoted by the arrow heads and magnitude by the arrow size, and the Gaussian source locations indicated by dots; center: plot of each reaction functions $\{r_{i,j}\}$; right: time $t = 0.5$ snapshot of a state realization with the observation locations indicated by circles.

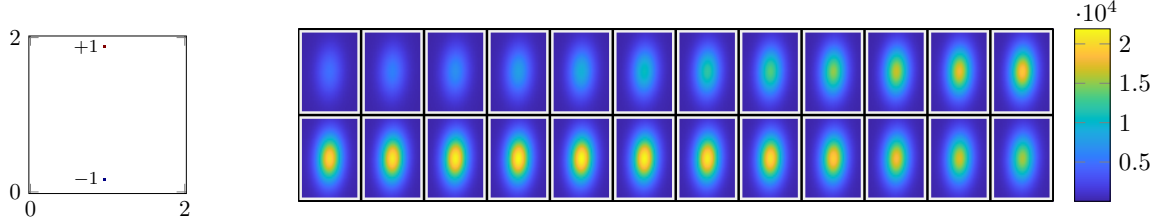


Figure 9. Visualizing the source and conductivity region for the DC Resistivity dataset. Left: The dipole source q in the $x_1 - x_2$ plane at the surface $x_3 = 1$. The dipole source is -1 at the coordinate $(1, \frac{1}{6})$ and is $+1$ at the coordinate $(1, \frac{11}{6})$, $q(x_1, x_2, x_3) = 0$ for $x_3 < 1$; right: Data generation of the DC Resistivity data set. We visualize the conductivity, m , to detect. Each image is a slice parallel to the x_1 - x_2 -plane. The top left is the surface, and left-to-right, top-to-bottom progresses down in depth.

where $\mathbf{x} = (x_1, x_2, x_3)$ and $\mathbf{Q}(y_3)$ is the 2×2 rotation matrix parameterized by the angle y_3 . We visualize one instance of the ellipsoidal conductivity region to detect in Figure 9.

We solve the PDE using a Finite Volume approach [23] with a rectangular mesh containing 48, 48, and 24 cells in each dimension, respectively.

The model parameters (the input data) $\mathbf{y} \in \mathbb{R}^3$ are generated by sampling from a uniform distribution on $[0, 1] \times [0.25, 3] \times [0, \pi]$. The target data $\mathbf{c} \in \mathbb{R}^{882}$ is generated by measuring the differences in the electric potential u at points in a uniform 21×21 rectangular grid in the x_1 - x_2 plane at the surface ($x_3 = 1$). Collecting the differences in the x_1 and x_2 directions at each of these 441 points gives $\mathbf{c} \in \mathbb{R}^{882}$. Because the data was generated with a large dipole source, we subtract the mean from all the samples so \mathbf{c} is the distinguishing features rather than the dominant source.